Influence of Extrusion on the Microstructure and Mechanical Behavior of Mg-9Li-3Al-xSr Alloys

YAN YANG, XIAODONG PENG, HAIMING WEN, BAOLONG ZHENG, YIZHANG ZHOU, WEIDONG XIE, and ENRIQUE J. LAVERNIA

Mg-9Li-3Al-xSr (LA93-xSr, x = 0, 1.5, 2.5, and 3.5 wt pct) alloys were cast and extruded at 533 K (260 °C) with an extrusion ratio of 28. The microstructure and mechanical response are reported and discussed paying particular attention to the influence of extrusion and Sr content on phase composition, strength, and ductility. The results of the current study show that LA93-xSr alloys contain both α-Mg (hcp) and β-Li (bcc) matrix phases. Moreover, the addition of Sr refines the grain size in the as-cast alloys and leads to the formation of the intermetallic compound (Al_4Sr). Our results show significant grain refinement during extrusion and almost no influence of Sr content on the grain size of the extruded alloys. The microstructure evolution during extrusion is governed by continuous dynamic recrystallization (CDRX) in the α-Mg phase, whereas discontinuous dynamic recrystallization (DDRX) occurs in the β-Li phase. The mechanical behavior of the extruded LA93-xSr alloy is discussed in terms of grain refinement and dislocation strengthening. The tensile strength of the extruded alloys first increases and then decreases, whereas the elongation decreases monotonically with increasing Sr; in contrast, hardness increases for all Sr compositions studied herein. Specifically, when Sr content is 2.5 wt pct, the extruded Mg-9Li-3Al-2.5Sr (LAJ932) alloy exhibits a favorable combination of strength and ductility with an ultimate tensile strength of 235 MPa, yield strength of 221 MPa, and an elongation of 19.4 pct.

I. INTRODUCTION

THE demand for lightweight metallic materials is fueled in part by the strategic need to reduce energy consumption while minimizing environmental impact. Under these constraints, Mg emerges as an attractive metal system, given its low density and attractive combination of physical and mechanical attributes. However, most of the commercially available Mg alloys possess an hcp crystalline structure and a high axial ratio (c/a) of 1.6236. Therefore, their capacity for plastic deformation is poor at room temperature, which consequently hinders the application of Mg alloys in many fields.[1,2] Interestingly, Li additions to Mg have been reported to not only decrease their density, but also enhance their ductility. On the one hand, alloying Mg with Li having extremely low density of 0.534 g/cm^3 can further reduce the density of Mg alloys. On the other hand, Li additions lead to a reduction of c/a axial ratio of the hcp lattice and even changes the crystalline structure of Mg alloys, which is beneficial in terms of ductility.[3,4] The Li content in Mg alloys is a key factor that influences both microstructure and mechanical response. The Mg-Li phase diagram[5] (as shown in the Appendix) indicates that when Li content is <5.5 wt pct, the Mg-Li alloy is composed of a single α-Mg phase with hcp structure which is Mg solid solution formed by Li dissolving in Mg. Alternatively, when 5.5 < wt pct Li < 11.5, a duplex alloy is formed containing both hcp-structured α-Mg phase and bcc-structured β-Li phase which is a Li solid solution formed by Mg dissolving in Li. When wt pct Li > 11.5 pct, the corresponding alloy consists exclusively of the bcc β-Li phase.[6,7] In the case of the hcp α-Mg phase, the Li addition leads to the reduction of c/a axial ratio of the hcp lattice such that the sliding systems are easy to activate.[3] The bcc β-Li phase has more active slip systems as compared to those in the hcp lattice. Therefore, the ductility of Mg-Li alloy is better than that of traditional Mg alloys.

In fact, Mg-Li alloys with low density, high specific stiffness, and good ductility are the lightest known metallic structural materials.[8–10] Not surprisingly, Mg-Li alloys have been used in the electrical, defense, and aerospace industries.[11,12] However, extensive application of Mg-Li alloys as structural materials has been hindered by their low strength, poor corrosion resistance, and limited thermal stability.[13,14] Strengthening of Mg-Li alloys via the introduction of alloying element represents an effective approach actively being studied and implemented. The

YAN YANG, Ph.D. Candidate, is with the College of Materials Science and Engineering, Chongqing University, Chongqing 400044, P.R. China, and also with the Department of Chemical Engineering and Materials Science, University of California, Davis, CA 95616. XIAODONG PENG and WEIDONG XIE, Professors, are with the College of Materials Science and Engineering, Chongqing University. HAIMING WEN and BAOLONG ZHENG, Postdoctoral Researchers, YIZHANG ZHOU, Assistant Researcher, and ENRIQUE J. LAVERNIA, Professor, are with the Department of Chemical Engineering and Materials Science, University of California. Contact e-mail: lavernia@ucdavis.edu

frequently used alloying elements include Al, Zn, rare earths (REs), and Si.[15–17] Al is a commonly studied alloying element because of its strengthening effect. Al in Mg-Li based alloys usually serves to improve the strength by means of precipitation and solid solution strengthening.[18,19] However, the strength of Mg-Li-Al alloys remains limited. For instance, the ultimate tensile strength (UTS) of Mg-8Li-1Al is only 150 MPa at room temperature, while that of Mg-14Li-1Al is only 135 MPa.[12] Therefore, it is necessary to introduce other strengthening elements. To this end, it has been reported that the addition of Sr into Mg-3Al-1Zn (AZ31), Mg-9Al-1Zn (AZ91), Mg-Sn, Mg-Al-Sn, and Mg-Ce-Mn-Zn alloys can improve their mechanical properties, especially at elevated temperatures.[20–23] However, review of the published literature shows that there is very limited information on the additions of Sr into Mg-Li or Mg-Li-Al alloys and their influence on microstructure and mechanical behavior. In addition to alloying, grain refinement *via* plastic deformation methods represents another recently studied approach to achieve improved strength in Mg-Li alloys. Deformation methods such as extrusion, rolling, and forging, have been used to further strengthen Mg-Li alloys.[13]

In view of the above discussion, the current study was motivated by two objectives. The first objective is to study the influence of hot extrusion on the microstructural evolution and mechanical behavior of Mg-Li-Al-Sr alloys. The second objective is to provide insight into the influence of Sr on the phase composition and mechanical behavior of Mg-Li alloys. To accomplish these objectives, the following approach was formulated and implemented. First, Mg-9Li-3Al-xSr (LA93-xSr) alloys with different compositions were cast under argon atmosphere, followed by extrusion at 533 K (260 °C) with an extrusion ratio of 28. The selection of these particular chemistries was based on the following factors. First, it has been reported that Mg-Li alloys possess a good combination of strength and ductility in the eutectic composition (5.5 < wt pct Li < 11.5).[24] A previous study indicated that ~3 wt pct Al content not only improves the strength but also helps retain its ductility in Mg-Li alloys.[3] Hence, on the basis of prior published studies, the Mg-9Li-3Al alloy was selected for our studies. Moreover, different amounts of Sr were added into Mg-9Li-3Al alloys in an effort to systematically study the influence of Sr additions. Microstructural studies were performed using scanning electron microscopy (SEM), transmission electron microscopy (TEM), scanning transmission electron microscopy (STEM), and X-ray diffraction (XRD). The tensile behavior of the hot extruded samples was then investigated on the basis of standard ASTM E8M testing methods, and the microhardness was also measured. The microstructural evolution during the hot extrusion is discussed with an effort to elucidate the underlying mechanisms governing mechanical behavior.

II. EXPERIMENTAL PROCEDURES

The starting materials used in this study are pure Mg (99.9 wt pct), pure Li (99.9 wt pct), and a Mg-8Sr

Table I. Chemical Composition of the Experiment Alloy (Wt pct)

Alloy Code	Nominal Composition	Actual Composition
LA93	Mg-9Li-3Al	Mg-8.51Li-3.02Al
LAJ931	Mg-9Li-3Al-1.5Sr	Mg-8.62Li-3.21Al-1.53Sr
LAJ932	Mg-9Li-3Al-2.5Sr	Mg-8.56Li-3.12Al-2.47Sr
LAJ933	Mg-9Li-3Al-3.5Sr	Mg-9.05Li-3.16Al-3.52Sr

master alloy (Mg 92 wt pct, Sr 8 wt pct). Target alloys were melted in vacuum melting furnace under the protection of argon atmosphere. The materials were first loaded in a graphite crucible which was mounted in a vacuum induction furnace. Then, the atmosphere in the furnace chamber was evacuated to 1×10^{-1} Pa, and the pressure in the furnace chamber was maintained at 1×10^{-1} Pa. Argon gas was introduced into the chamber to ensure a protective atmosphere prior to melting, and the Ar pressure was maintained at standard atmospheric pressure during melting. The melt was maintained at 953 K (680 °C) for 30 minutes, and no stirring was used. Then, the melt was cast in a permanent mold $\Phi 90 \times 300$ mm, which was preheated at 523 K (250 °C) to obtain the as-cast specimens (Mg-9Li-3Al-xSr). The as-cast specimens were machined from $\Phi 90$ to $\Phi 80$ mm. A homogenization treatment was carried out at 533 K (260 °C) for 12 hours in a vacuum furnace. The atmosphere in the heat-treatment furnace chamber was evacuated to 1×10^{-1} Pa, and then the argon gas was introduced and maintained at atmospheric pressure during homogenization. The specimens were extruded at 533 K (260 °C) from $\Phi 80$ to $\Phi 15$ mm with an extrusion ratio of 28. Chemical composition of the alloys was measured by atomic absorption spectrometry (aas) using a Hitachi Z-8000 atomic absorption spectrophotometer, and measured compositions are shown in Table I. Sample designations corresponding to alloys with 9 wt pct Li and 3 wt pct Al are LA93, LAJ931, LAJ932, and LAJ933 based on the different Sr amounts (0, 1.5, 2.5 and 3.5 wt pct), respectively.

The microstructure of the as-cast and extruded samples was studied using JEOL JSM 6460LV SEM. The SEM samples were prepared using standard mechanical grinding and polishing procedures followed by etching using 2 vol. pct HNO_3 alcohol solution etchant. The SEM images were acquired using secondary electrons (SE) detector. Local chemical analysis was performed using a Genesis 7000 energy dispersive spectroscopy unit. Phase analyses of the materials were conducted using X-ray diffraction a D/MAX-2500pc diffractometer, using CuKα radiation at 45 kV, 40 mA with an initial angle of 10 deg, a final angle of 90 deg and a step size of 0.02 with ~1 seconds per step. The XRD data was analyzed using the ICDD database. The microstructure of the extruded LAJ932 alloy was investigated in detail using transmission electron microscopy, based on its favorable combination of strength and ductility. The TEM specimens were prepared by mechanically grinding and dimpling the thin foils to a thickness of 20 μm, followed by additional

thinning to electron transparency using a Gatan PIPS 691 ion milling system. The TEM and STEM observations were carried out on a JEOL 2500SE TEM/STEM microscope operating at 200 kV. Selected area electron diffraction (SAED) patterns were recorded using apertures with a diameter of 100 or 200 nm. Grain size measurements were conducted using an Olympus analySIS FIVE software using the following procedure. First, a contour was drawn along the boundary of the grain, and the software automatically provided the mean diameter of the grain by measuring and averaging 180 diameters for angles in the range 0 through 179 deg with a step width of 1 deg for each grain size measurement. The coarse grains were measured from SEM images, whereas the ultrafine grains were measured from TEM images. High resolution TEM (HRTEM) images of lattice fringes were taken by JEOL 2500SE to determine the dislocation density in α-Mg phase. Three α-Mg grains in extruded LAJ932 alloy were imaged to obtain the dislocation density. Inverse Fourier transformation was performed on an HRTEM image to obtain the $(1\bar{1}01)$ crystallographic planes, and the number of dislocations in the image was counted. The same procedure was carried out for all the 60 HRTEM images, and the dislocation density was determined by dividing the average number of dislocations per image by the area of an image.

Tensile specimens with gauge dimensions of $30 \times \Phi6$ mm were machined from the central regions of the extruded rods with the gauge axes parallel to the extrusion direction following ASTM E8M. Tensile tests of extruded LA93-xSr alloy were performed on a CMT-5105 (SANS Materials Analysis Inc., Shenzhen, China) tensile tester with a displacement speed of 1 mm/min. The stress–strain curves were recorded for each specimen, and these curves were used to determine the 0.2 pct proof strength (yield strength, YS), UTS, and elongation to failure (elongation, δ). The reported strength and elongation for each sample are based on the averages of three parallel tests. The Vickers hardness values were measured using a test load of 100 g, and ten indentations per sample were made for each hardness measurement reported. The fracture morphology was observed by JEOL JSM 6460LV SEM.

III. RESULTS

A. *Microstructure*

1. *Microstructure of As-cast LA93-xSr alloys*
The microstructure of the as-cast $\Phi90$ mm alloys ingots is shown in Figure 1. The micrographs show that LA93-xSr alloys contain both hcp α-Mg phase and bcc β-Li phase. The α-Mg phase includes primary α-Mg and eutectic α-Mg. The dark areas in Figure 1 are primary α-Mg, while the gray areas are eutectic structure containing both eutectic α-Mg and β-Li phase. The bright phase in the eutectic area is the β-Li phase, which has both equiaxed and rod-like grains. The primary α-Mg grains of LA93 alloy are ~140 μm, whereas the grain size of eutectic α-Mg is ~3 μm. In the case of the β-Li phase, the equiaxed grains are ~1 μm in diameter, while the rod-like grains are ~1 μm in diameter and ~5 to 10 μm in length. With the addition of Sr, new intermetallic compound, with fishbone-like morphology, is found in the alloys and the amount of the compound increases with the increase of Sr content. It can also be observed that with the addition of Sr, the grain sizes of α-Mg and β-Li phases are reduced. When containing 1.5 wt pct Sr, the primary α-Mg grains of the as-cast alloys are ~100 μm which are much finer than those in the LA93 alloy. However, the primary α-Mg grains increase to 130 μm when Sr content is increased to 2.5 wt pct. The rod-like grains of the β-Li phase disappear and only equiaxed grains are present in alloys with the addition of Sr. There is no significant change in the grain size of eutectic α-Mg with the Sr additions. The distribution of the new intermetallic compound in the as-cast alloys with Sr additions is heterogeneous and continuous. The grains of the as-cast alloys are generally coarse.

2. *Microstructure of the extruded LA93-xSr alloys*
Hot extrusion at 533 K (260 °C) using an extrusion ratio of 28 is used to refine the microstructure of the as-cast LA93-xSr alloys. Figure 2 shows the microstructure of extruded alloys vertical to the extrusion direction. It can be seen that the grains in the extruded alloys are much finer than those in the corresponding as-cast alloys. The grains of the primary α-Mg were refined from ~100-140 μm to ~5-20 μm, the grain size of eutectic α-Mg is from ~0.2 to 2 μm, and the β-Li phase only has equiaxed grains with size from ~0.2 to 0.4 μm. Note that the small grain sizes of the eutectic α-Mg and the β-Li phase are confirmed by following TEM investigations. The intermetallic compound contains approximately equiaxed particles with size from ~2 to 15 μm, which are nearly homogeneously distributed, the original fishbone-like morphology in the as-cast alloys being fractured and dispersed. With different Sr additions, there is no significant change in the grain size of the primary α-Mg, eutectic α-Mg and β-Li phase in the extruded alloys. With increasing Sr content, the volume fraction of the intermetallic compound and the particle size of the compound in the extruded alloys both increase. The microstructure parallel to the extrusion direction is shown in Figure 3. The micrographs indicate that the α-Mg phase is elongated along the extrusion direction. The particles of the intermetallic compound phase are mainly distributed on the α/β phase interface and in eutectic areas. Figure 4 shows the TEM images of LAJ932 alloy. The boundaries of the α-Mg grains in extruded LAJ932 alloy are irregular, and the dislocation density in the grains is apparently high, as shown in Figures 4(a) and (b). In contrast, the grain boundaries of β-Li grains are sharp and straight, and the grain interiors are very clean, indicating very few dislocations as shown in Figures 4(d) and (e). Note that Figures 4(c) and (f) show diffraction patterns which confirm that the structure is hcp and bcc, respectively. In order to confirm the high dislocation density in α-Mg phase, HRTEM was used to study dislocation densities. During
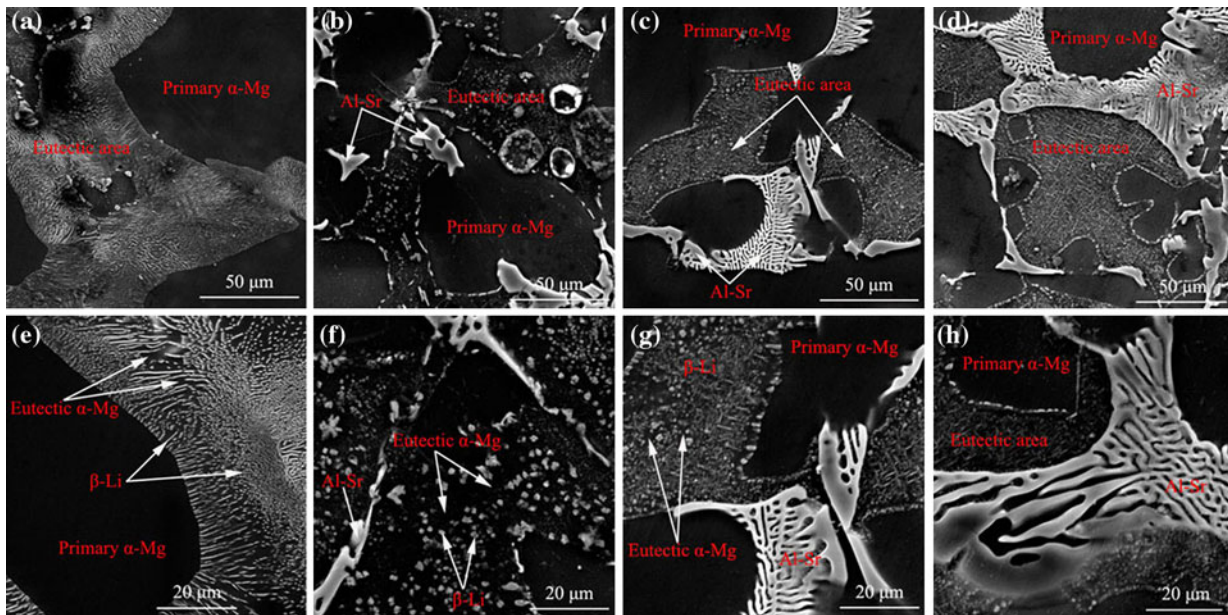
Fig. 1—Microstructure of as-cast Φ90 mm LA93-*x*Sr alloys: (*a, b*) LA93, (*c, d*) LAJ931, (*e, f*) LAJ932, (*g, h*) LAJ933.
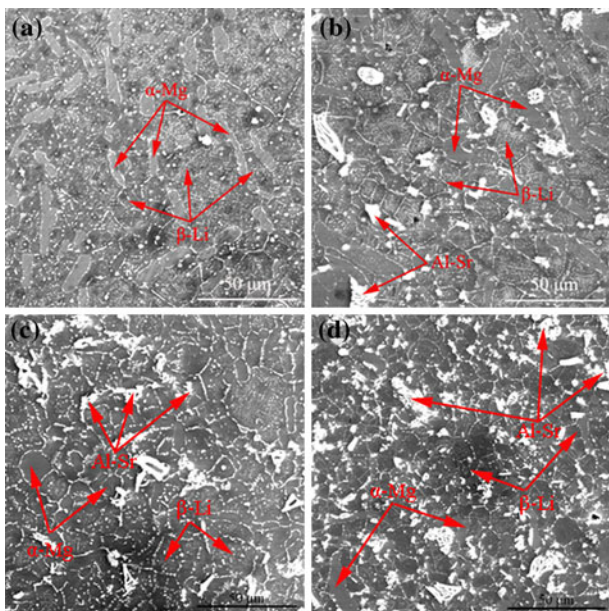

Fig. 2—SEM morphology of extruded LA93-*x*Sr alloys (perpendicular to the extrusion axis): (*a*) LA93, (*b*) LAJ931, (*c*) LAJ932, and (*d*) LAJ933.
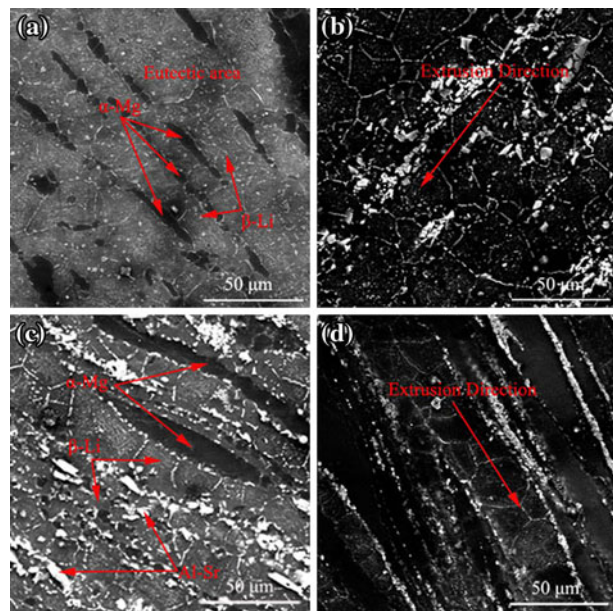

Fig. 3—SEM morphology of extruded LA93-*x*Sr alloys (parallel to the extrusion axis): (*a*) LA93, (*b*) LAJ931, (*c*) LAJ932, and (*d*) LAJ933.

this investigation, HRTEM images of three α-Mg grains were recorded for the extruded LAJ932 alloy. Figure 5 presents HRTEM images of the extruded LAJ932 alloy to show the steps undertaken to obtain the dislocation density. Figure 5(a) shows a typical CDRX α-Mg grain and its diffraction pattern on the $[\bar{1}2\bar{1}3]$ zone axis, Figure 5(b) depicts a representative lattice-fringe image, and Figure 5(c) presents the $(1\bar{1}01)$ planes obtained by inverse Fourier transformation of Figure 5(b) with six dislocations marked by "T" at the dislocation cores. The dislocation density was determined by dividing the average number of dislocations per image by the area

of an image. The dislocation density in $(1\bar{1}01)$ planes of α-Mg phase in the extruded LAJ932 alloy is 1.38 × 10^{16} m^{-2} which is relatively high.

Figure 6 shows the SEM morphology and EDS point analysis of the extruded LAJ932 alloy. The α-Mg phase and the β-Li phase are identified. EDS was performed at a specific location which was labeled as A in the compound area. The results show that Mg, Al, and Sr elements exist in this region. Because the particle size of the compound is only ~2.5 μm and the spot size and the interaction volume of the electron beam of the JEOL JSM 6460LV SEM at 20 kV with tungsten filament are
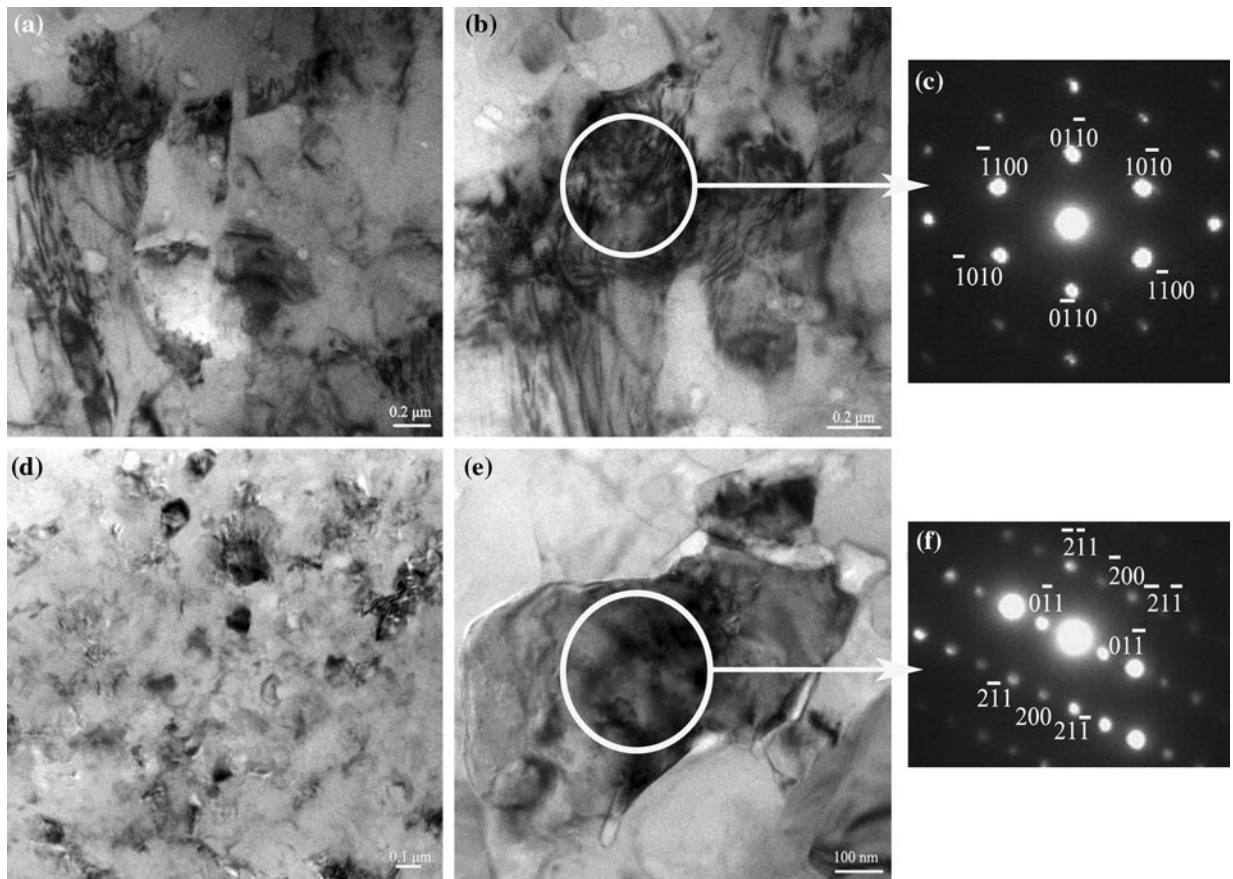
Fig. 4—TEM images of extruded LAJ932 alloy: (*a*, *b*) TEM images showing α-Mg phase, (*c*) Diffraction pattern of α-Mg phase, (*d*, *e*) TEM images showing β-Li phase, and (*f*) Diffraction pattern of β-Li phase.
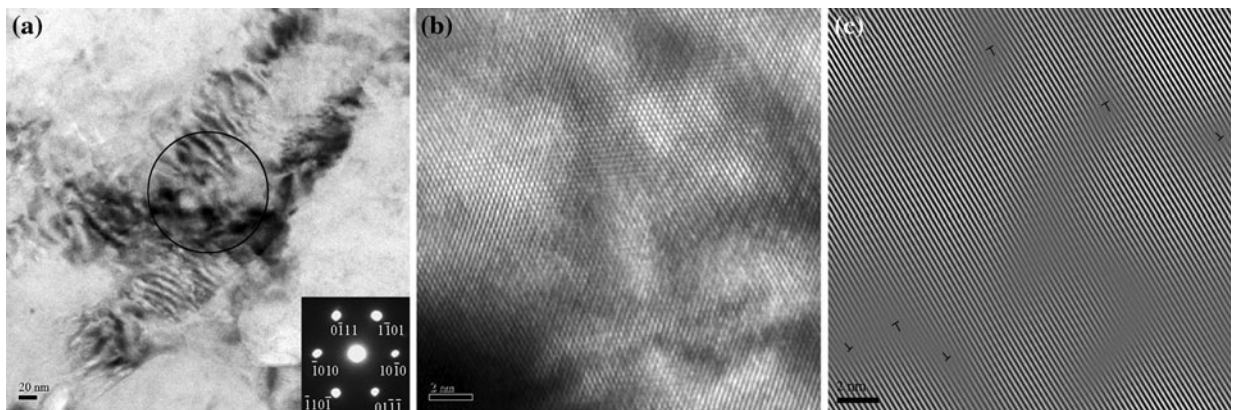

Fig. 5—(*a*) A typical CDRX α-Mg grain in the extruded LAJ932 alloy and its SAED pattern on the $[1\bar{2}\bar{1}3]$ zone axis; (*b*) a lattice-fringe image of the grain in (a); and (*c*) the $(1\bar{1}01)$ crystallographic planes obtained by inverse Fourier transformation of (b), with dislocation marked by "T" at the dislocation cores.

on the same order as the particle size, Mg is also detected. Figure 7 shows the SEM and EDS elemental mapping analyses of the extruded LAJ932 alloy. Al and Sr maps show a high concentration of Al and Sr in the intermetallic compound area. From the Mg map, it can be seen that the Mg amount in the compound areas is less than that corresponding to other regions. It is also observed that the brightness of the β-Li phase areas exceeds that of the areas of the α-Mg phase, suggesting that the amount

of Mg in the β-Li phase is less than that in the α-Mg phase. Note that complete bright contrast indicates absence of the element, and *vice versa*. A Li map was not established given that Li cannot be detected by EDS.

XRD patterns of extruded LA93 and LAJ932 alloys are presented in Figure 8. The results indicate that the LA93 alloy is composed of α-Mg, β-Li, and $Mg_{17}Al_{12}$ phases, whereas the LAJ932 alloy consists of α-Mg, β-Li, $Mg_{17}Al_{12}$, and Al_4Sr phases. Based on the EDS
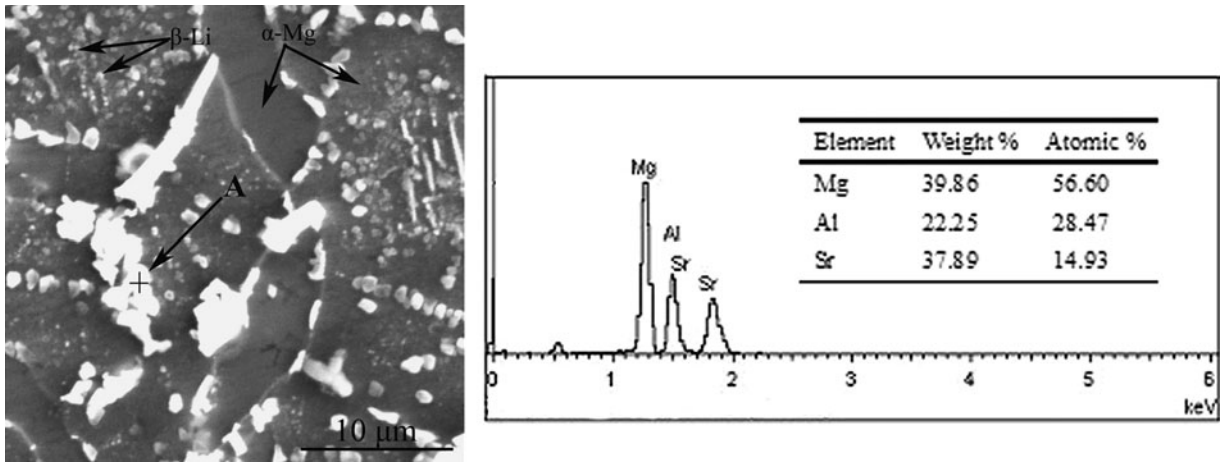
Fig. 6—SEM morphology and EDS result of extruded LAJ932 alloy.

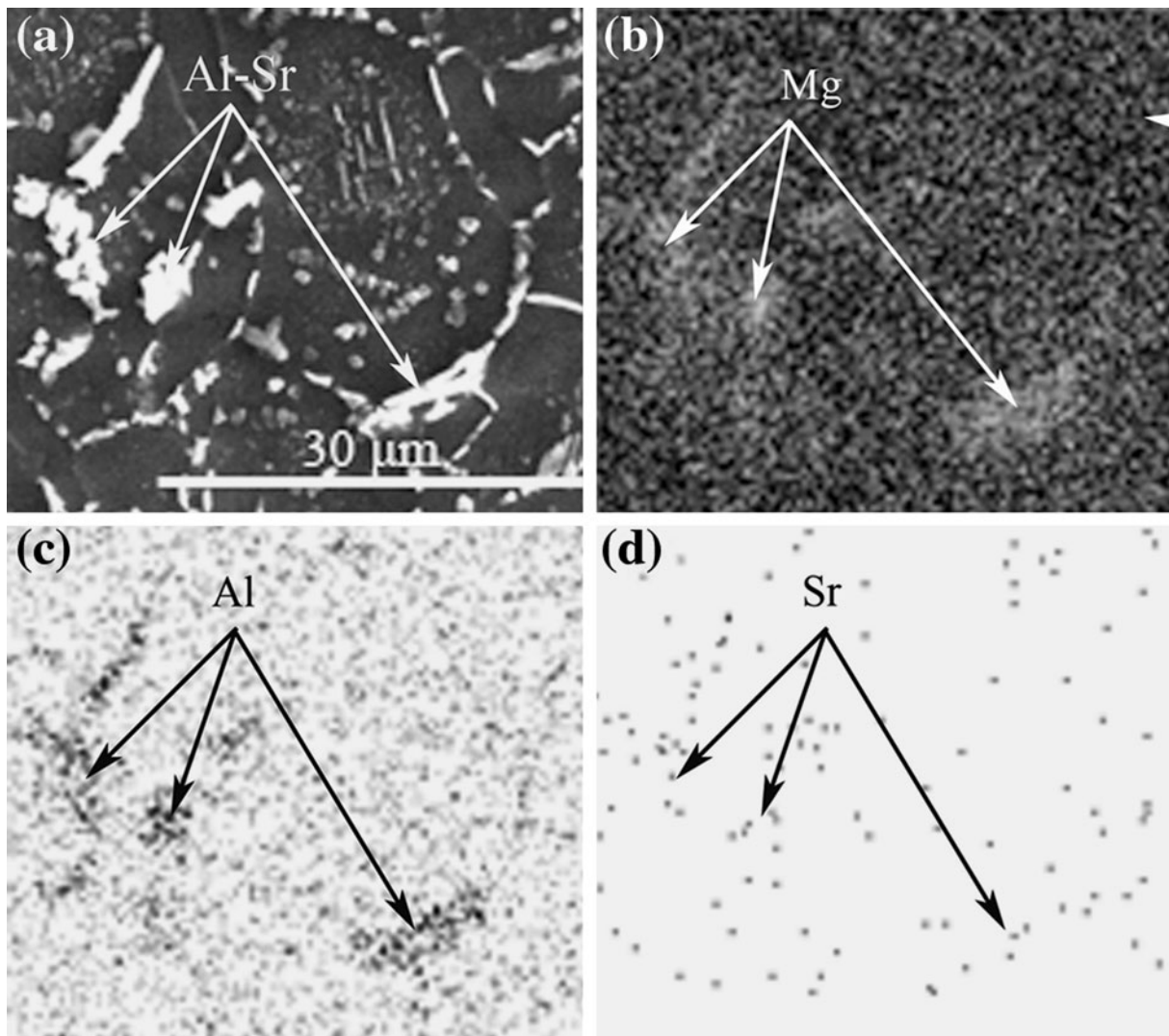| Element	Weight %	Atomic %
Mg	39.86	56.60
Al	22.25	28.47
Sr	37.89	14.93

Fig. 7—SEM and EDS map analysis of extruded LAJ932 alloy: (*a*) SEM image, (*b*) Mg, (*c*) Al, and (*d*) Sr.
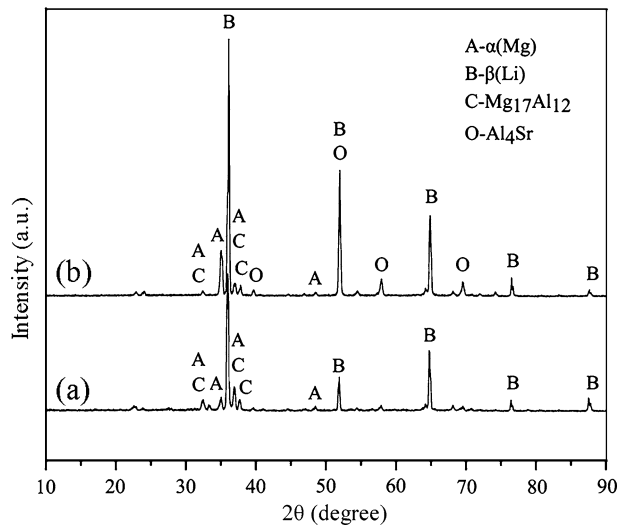
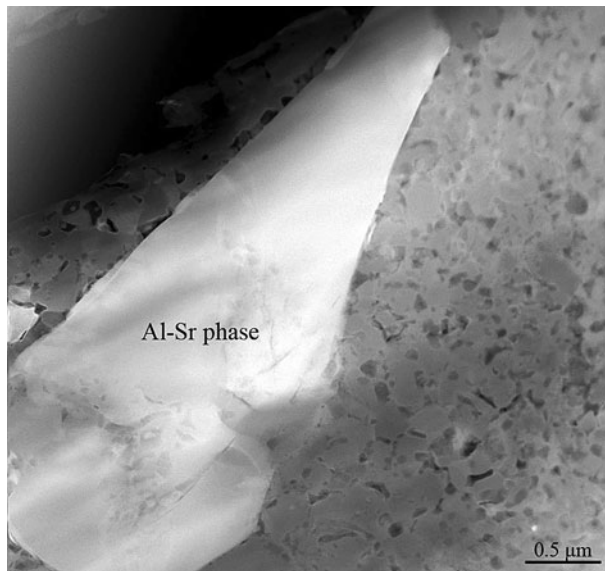Fig. 8—XRD patterns of extruded LA93-xSr alloys: (a) LA93 and (b) LAJ932.

Fig. 9—STEM image showing Al-Sr phase.

and XRD results, it can be concluded that the white intermetallic compound in the SEM images is the Al_4Sr phase. Most of the Al_4Sr phase is distributed at the interfaces between primary α and β phases as well as in the eutectic areas, as shown in Figures 2 and 3.

Figure 9 is a STEM image showing the intermetallic compound from the LAJ932 alloy. The bright area in the image is an Al_4Sr particle. Note that the presence of bright contrast in a STEM image indicates a higher atomic number and/or a larger thickness of the area.

B. Mechanical Properties

The tensile properties of the extruded alloys with different Sr content are presented in Table II. As three tensile tests were performed for each material, representative engineering stress–strain curves are presented for

Table II. Mechanical Properties of Extruded LA93-xSr Alloys

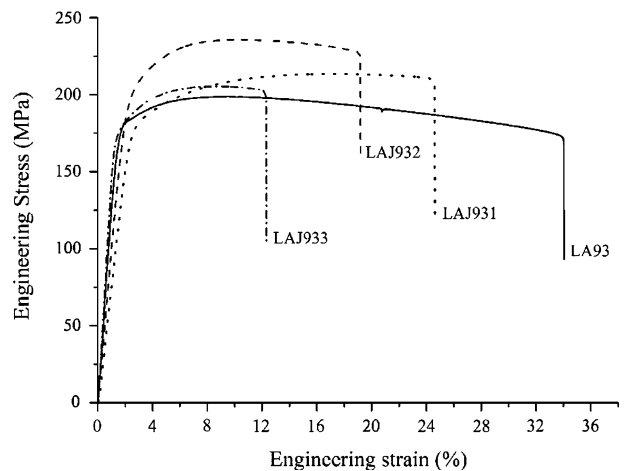| Alloy Code	Yield Strength (MPa)	Ultimate Strength (MPa)	Elongation (Pct)
LA93	192 ± 3	200 ± 5	34.5 ± 1.1
LAJ931	201 ± 5	215 ± 6	24.7 ± 0.8
LAJ932	221 ± 6	235 ± 7	19.4 ± 1
LAJ933	190 ± 4	206 ± 3	12.1 ± 1.3

Fig. 10—Tensile stress–strain curves of extruded LA93-xSr alloys.

each extruded alloy as shown in Figure 10, and the mean values and the associated errors are summarized in Table II. A general trend is that both the UTS and yield strength of alloys increase first and then decrease with increasing Sr content. The extruded LAJ932 alloy containing 2.5 wt pct Sr has the maximum tensile strength of 235 ± 7 MPa, which is 21.2 pct higher than that of LA93 alloy, and yield strength of 221 ± 6 MPa which is 18.3 pct higher than that of LA93 alloy. The LA93 alloy possesses the largest elongation measured in this study (34.5 ± 1.1 pct), and that of LAJ932 alloy is 19.4 ± 1 pct. Comparatively, LAJ932 alloy possesses a favorable combination of strength and ductility. Figure 11 shows the microhardness of the extruded LA93-xSr alloys. The hardness of the alloys increases with the increase of Sr content. LAJ933 alloy containing the highest Sr content possesses the highest hardness. Figure 12 shows the HV microhardness of α-Mg, β-Li, and Al_4Sr phases in LAJ932 alloy which are 94.2 ± 3, 74.1 ± 3 and 122.5 ± 6, respectively. Thus, the Al_4Sr compound, having the highest hardness value, can be considered as a strengthening phase in the alloys.

C. Fracture Morphology

Figure 13 shows the fracture morphology of the extruded alloys. The fracture surface of LA93 alloy consists of uniformly sized dimples (as shown in Figure 13(a)), typical of a ductile fracture, which is consistent with the good ductility of the alloy. With the addition of Sr, although dimples still exist on the
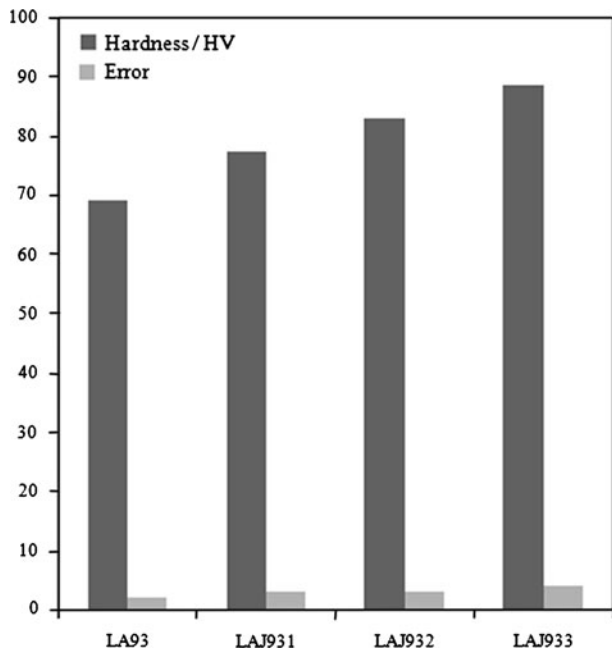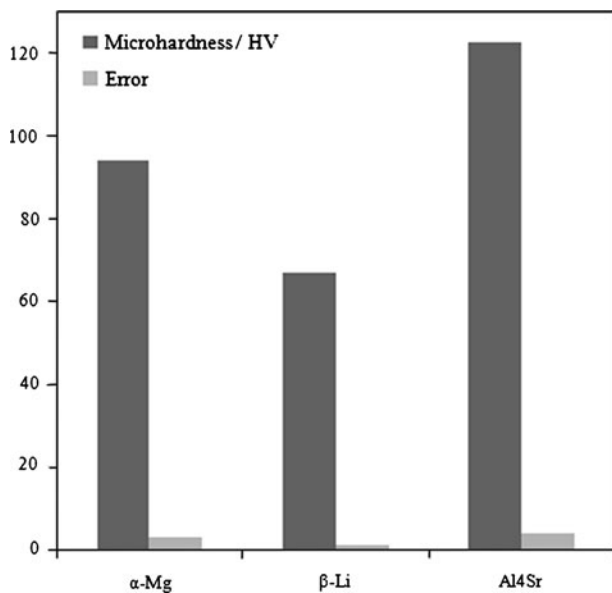
Fig. 11—Microhardness of extruded LA93-xSr alloys.

Fig. 12—Microhardness of α-Mg, β-Li, and Al₄Sr phases in extruded LAJ932 (Mg-9Li-3Al-2.5Sr) alloy.

fracture surfaces, some tear ridges caused by Al₄Sr are present. Overall, the fracture mechanism of LA93-xSr alloys is mostly that of ductile fracture which is consistent with the relatively high ductility that was documented in tension.

IV. DISCUSSION

A. Phase Composition in LA93-xSr Alloy

The LA93 alloy contains both primary α-Mg and a eutectic structure as shown in Figures 1(a), (b), and 2(a).

The Li content of LA93 alloy is around 9 wt pct which falls in the eutectic region (see the Mg-Li binary phase diagram). Therefore, the presence of primary α-Mg, eutectic α-Mg, and eutectic β-Li phases in the LA93 alloy is consistent with the Mg-Li phase diagram (see phase diagram in Appendix).

The EDS and XRD results confirm that the addition of Sr will lead to the precipitation of the Al₄Sr phase, consistent with observations. The solid solubility of Sr in Mg is only about 0.11 wt pct[5] which is quite low, and therefore, most of the Sr will be present in the form of intermetallics. On the basis of the electronegativity difference between elements, the trends for compound formation can be estimated. The electronegativity difference between Sr and Al is 0.66, while that between Sr and Mg is 0.36.[25] Therefore, it is easier for Al than for Mg to react with Sr. The formation of Al₄Sr phase is further confirmed on the basis of the Al-Sr binary phase diagram[5] and also consistent with a study related to the addition of 0.8 wt pct Sr into an AZ31 alloy.[26]

B. Microstructure Evolution During Hot Extrusion and Influence of Sr

1. Microstructure evolution during hot extrusion

The grains in the extruded alloys are significantly refined during hot extrusion. The LA93-xSr alloys contain both α-Mg and β-Li matrix phases. The different microstructural characteristics associated with the α-Mg and the β-Li phases, as shown in Figures 2 through 4, indicate that the mechanisms for microstructural refinement during the hot extrusion process are different. The α-Mg and β-Li phases exhibit significant differences in physical properties, such as melting point, ductility, and crystal structure; therefore, their behavior during extrusion is anticipated to be different, consistent with the microstructures shown in Figures 2 through 4. The characteristics of these two phases are discussed next.

a. α-Mg phase. The α-Mg phase is elongated along the extrusion direction as shown in Figure 3. The TEM images of extruded LAJ932 alloy in Figure 4 show that the grain boundaries of α-Mg grains are irregular and that the dislocation density in the grain interiors is high, which indicates that deformation-induced grain refinement has occurred in the α-Mg phase. The microstructure evolution during extrusion starts with the subdivision of grains into dislocation cells which are formed through deformation-induced dislocation accumulation and recombination.[27] As deformation proceeds, the dislocation cell boundaries are transformed into low-angle subgrain boundaries, followed by transformation of low-angle boundaries into high-angle boundaries with the further increase of strain.[27–30] This series of strain-induced grain refinement processes are sometimes referred to as continuous dynamic recrystallization (CDRX).[31] Typically, the CDRX mechanism is favored at lower temperature, and an increase in the deformation temperature will slow down CDRX, because dislocation recovery is enhanced with increasing temperature.[30] Pure Mg has a medium stacking fault energy which is ~60-78 mJ/m².[32] There-
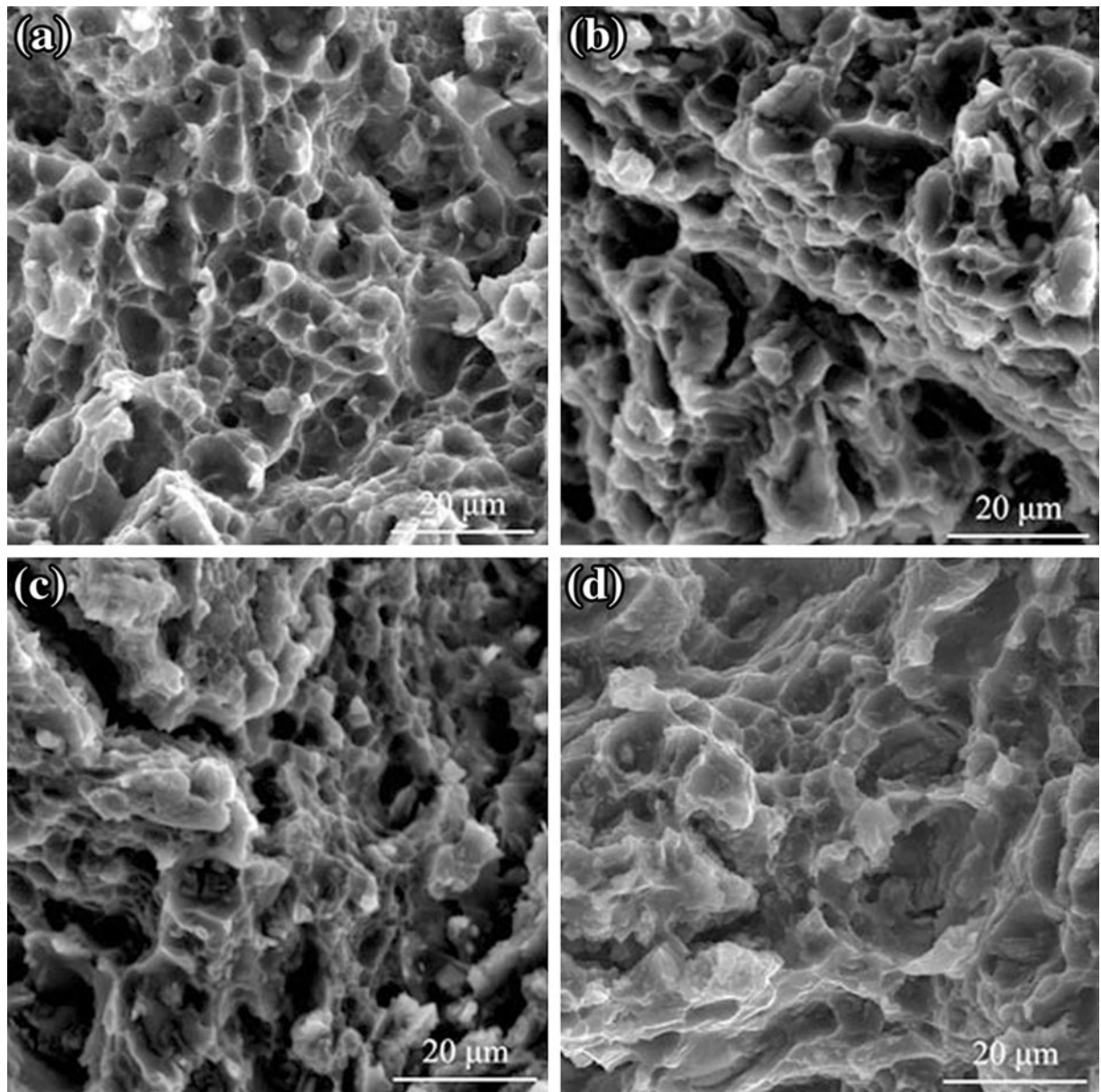
Fig. 13—Fracture morphology of extruded LA93-xSr alloys: (a) LA93, (b) LAJ931, (c) LAJ932, and (d) LAJ933.

fore, discontinuous dynamic recrystallization (DDRX) may occur during deformation at sufficiently high temperatures. However, strain is also an important factor that affects CDRX allowing it to occur, even at relatively high temperatures in Mg alloys. In related studies, Miura et al.[33] argued that CDRX occurs in Mg-6Al-1Zn alloy during hot compression at 623 K (350 °C) under high strain conditions. Similarly, a study by X. Yang et al.[34] shows that CDRX occurs in AZ31 Mg alloys during hot deformation. Yi et al.[35] and Yang et al.[36] proposed that CDRX is one of the most important DRX mechanisms in Mg and Mg alloys. Hence, on the basis of our results, and those from the published literature, we propose that CDRX is the dominant mechanism for microstructural refinement in α-Mg phase at the extrusion temperature of 533 K (260 °C) with an extrusion ratio of 28. Strain-induced grain refinement or CDRX

usually leads to high dislocation density in the grain interiors and irregular grain boundaries with excessive dislocations which are known as non-equilibrium grain boundaries.[37] In addition, during the early stages of CDRX, grains may be elongated along the deformation direction. This phenomenon is common during some (severe) plastic deformation techniques which involve CDRX such as equal-channel angular pressing and extrusion.[37] Therefore, the microstructural features observed from SEM and TEM for α-Mg phase are consistent with the microstructural characteristics widely reported for CDRX.

b. *β-Li phase.* TEM images of the β-Li phase show that the grain boundaries are sharp and that there are few dislocations inside the grains, which are typical attributes of grains generated by DDRX, characteristic of

dynamic recrystallization.[38] The processes of nucleation and grain growth are involved in DDRX.[39,40] Formation of nuclei predominantly occurs at pre-existing grain boundaries, twin boundaries, and deformation bands that have sufficient stored strain energy.[41,42] The DDRX then proceeds through the growth of new nucleated grains by migration of their grain boundaries, thereby leading to the consumption of the deformed matrix. The recrystallized grains have sharp and straight equilibrium grain boundaries and are relatively depleted of dislocations in the grain interiors. The β-Li grains in the extruded alloys have these microstructural characteristics as shown in the TEM images. Hot plastic deformation with DDRX can lead to significant grain refinement.[43,44] In order to initiate DDRX, some critical strain is necessary. The smaller the degree of deformation, the higher the temperature is required to initiate the recrystallization.[45–47] In general, DDRX is favored at higher temperatures, which accelerates the diffusion-controlled processes and facilitates the migration of grain boundaries over large distances.

Usually, the metals with bcc structure have higher stacking fault energy;[48] hence, dynamic recovery of dislocations by climb or cross-slip will readily occur, thereby inhibiting DDRX. However, in the case of the LA93-xSr alloys, the α-Mg phase and the compound distributed along the α/β phase interfaces anchor the movement of dislocations in the β-Li phase, thereby hindering dynamic recovery in the β phase and facilitating DDRX. In addition, the β-Li phase with bcc structure is softer and has better ductility than that of the α-Mg phase. Therefore, plastic deformation occurs first in the β-Li phase during extrusion thus making it easy for the β-Li phase to reach a critical strain for DDRX. In essence, the α-Mg phase and the compound Al_4Sr phase facilitate DDRX of the β-Li phase. Furthermore, the melting point of the β-Li phase is relatively low [861 K (588 °C) in eutectic region],, and the extrusion temperature of 533 K (260 °C) is high enough to meet the temperature requirement of DDRX. In summary, DDRX is proposed to be responsible for the formation of β-Li grains with sharp grain boundaries in the extruded alloys that are significantly finer than those in the as-cast alloys.

c. Al₄Sr. The Al_4Sr phase will experience only limited plasticity during deformation. Its hardness and inherent brittleness[49] will lead to fracture and dispersion of the starting fishbone-like network into particles, as shown in Figures 2 and 3. The size and distribution of the Al-Sr phase in the extruded material are thought to contribute positively to mechanical behavior; details are discussed in a subsequent section.

2. *Effect of Sr content on the microstructure of extruded LA93-xSr alloys*

The effect of Sr on the microstructures of the α-Mg and the β-Li phases in the extruded LA93-xSr alloys is not significant, as shown in Figures 2 and 3. The CDRX occurs in the α-Mg phase, whereas DDRX operates in the β-Li phase during hot extrusion. Therefore, the

extruded alloys have much finer grains than those of the as-cast alloys. Moreover, the influences of the Al_4Sr phase on the extent of grain refinement by CDRX in the α-Mg phase and DDRX in the β-Li phase are not significant. Although it facilitates the DDRX process in the β-Li phase, the Al_4Sr phase does not influence the ultimate grain size of the recrystallized β-Li grains. Therefore, with different Sr contents (or different amounts of Al_4Sr), there is no significant change in the grain size of α-Mg or β-Li phases in the extruded LA93-xSr alloys.

C. *Strengthening Mechanisms in Extruded LA93-xSr Alloys*

In general, strengthening strategies used for Mg-Li alloys, such as alloying and severe plastic deformation processing, reportedly fail to attain UTS values that are higher than 200 MPa.[50] However, the results of the current study show that the yield strength of extruded LAJ932 alloy reaches 221 ± 6 MPa, with elongation values that are significantly higher than that of most conventional Mg alloys. The strengthening mechanisms that are active in the extruded LA93-xSr alloys are discussed as follows.

1. *Effect of Extrusion on the Mechanical Properties of Extruded LA93-xSr Alloys*

The mechanical properties of the as-cast LA93-xSr alloy were reported in a previous published article.[51] The as-cast LA93 alloys possess a tensile strength of 125 MPa, a yield strength of 92 MPa, and an elongation of 14.6 pct, whereas the as-cast LAJ932 alloy exhibits a tensile strength of 186 MPa, a yield strength of 149 MPa, and an elongation of 8.4 pct. Compared with the as-cast alloys, the yield strength of extruded LA93 and LAJ932 alloys increases by 108.8 ± 3.2, and 48.3 ± 4.0 pct, respectively because of the extrusion, which means that extrusion plays an important role in the improvement of mechanical behavior in the LA93-xSr alloys. The influences of extrusion on the mechanical properties include several aspects.

a. Grain boundary strengthening. Dynamic recrystallization leads to grain refinement during extrusion, and hence, the grains in the extruded alloys are much finer than those in the corresponding as-cast alloys. On the basis of the Hall–Petch relationship,

$$\Delta\sigma_{bs} = kd^{-1/2} \qquad [1]$$

where k is a constant ($= 0.28$ MN m$^{-3/2}$ for Mg[52]), and d is the mean grain size, one can estimate the contributions from grain boundary strengthening mechanism. According to Eq. [1], the grain size has a noticeable influence on yield strength. Take the primary α-Mg phase as an example; the grains of the primary α-Mg were refined from ~100-140 μm to ~5-20 μm because of extrusion as mentioned in Section III–A. The calculated strength of α-Mg in the as-cast alloy due to grain boundaries strengthening ranges from ~23.7 to 28 MPa, while that in the extruded alloy from ~62.6 to 120 MPa.

Thus, the strength of the primary α-Mg phase increases at least by 34.6 MPa because of grain refinement. Thus, it is inferred that the grain refinement plays an important role in the measured tensile properties.

b. Dislocation strengthening. Despite dynamic recrystallization being operative during extrusion, TEM results revealed a relatively high dislocation density at α-Mg grain interiors in the extruded alloys because of CDRX. It then follows that one may implement the Taylor equation,

$$\sigma_{ds} = M\alpha G b \rho^{1/2} \qquad [2]$$

where M is Taylor factor, α is a constant, G is the shear modulus, b is the Burgers vector, and ρ is the dislocation density to estimate the contributions to strength that are derived from dislocations. If one considers the dislocation density in $(1\bar{1}01)$ planes of α-Mg phase as an example, then the dislocation density in $(1\bar{1}01)$ planes of α-Mg in the extruded LAJ932 alloy is $\sim 1.38^{+1.8}_{-1.0} \times 10^{16}\,\mathrm{m}^{-2}$ estimated according the HRTEM images, per the procedure described above. In related studies,[53] the dislocation density in $(1\bar{1}01)$ plane of α-Mg in the as-cast Mg alloy is $\sim 2.8^{+0.7}_{-1.4} \times 10^{15}\,\mathrm{m}^{-2}$. Therefore, it is inferred that the dislocation density in $(1\bar{1}01)$ plane of α-Mg is high because of extrusion which means the dislocation density in α-Mg of the extruded alloy is higher than that in the as-cast alloy. Based on Eq. [2], once can anticipate that the measured high dislocation density will indeed contribute to the observed increase in yield strength; however, we are only able to affirm so qualitatively. As a result of the hcp structure of the α-Mg phase, the Burgers vector in different crystallographic planes varies leading to uncertainty in the magnitude of α in Eq. [2], and hence, we are unable to report on a precise value for dislocation strengthening in the extruded alloy.

In addition, during the extrusion process, defects such as gas-pore and inclusions that may have been present in the as-cast material are generally reduced, leading to an overall enhancement in mechanical behavior.

2. Effect of Sr content on mechanical properties of extruded LA93-xSr alloys

The strength of extruded LA93-xSr alloys first increases and then decreases with increasing Sr content. The LAJ932 alloy containing 2.5 wt pct Sr exhibited the maximum strength value for the alloys studied herein. The elongation of LA93-xSr alloys decreases, whereas the hardness increases with increasing Sr content as shown in Figures 10, 11 and Table II.

With the addition of Sr, the Al$_4$Sr phase was formed as discussed in a previous section. The Al$_4$Sr phase, with the highest hardness measured among all phases (see Figure 12) can be considered as a strengthening phase in the alloys. The Al$_4$Sr particles exhibit a size from ~2 to 15 μm, and hence one can discuss mechanical behavior by considering LA93-xSr as a particulate-reinforced metal matrix composite (MMC) system. On the basis of the theory of particulate strengthening,[54] the strength can be estimated from the following equation[55]:

$$\sigma = f_m \sigma_m + f_h \sigma_h \qquad [3]$$

where σ, σ_m, and σ_h are the strengths of LA93-xSr alloy, LA93 matrix alloy, and Al$_4$Sr phase, respectively; f_m and f_h are the volume fractions of matrix alloy and Al$_4$Sr particulates, respectively. As, volume fraction of Al$_4$Sr (f_h) increases with increasing Sr content, it then follows that strength and hardness also increase with increasing amount of Sr. The increases in strength and hardness are accompanied by a decrease in ductility, as the hard and rigid Al$_4$Sr phase severely restricts deformation of the adjacent softer α-Mg and β-Li phases. However, too much Sr in LA93-xSr alloys is likely to cause aggregation of the Al$_4$Sr phase which will lead to stress concentration and ultimately fracture initiation at the interfaces between Al$_4$Sr and matrices during tensile deformation, and hence, decrease in tensile strength.[56] However, the microhardness is less influenced by the size and dispersion of Al$_4$Sr for two reasons. First, as indentation is performed on localized regions of the materials, this renders the measurements less sensitive to particle dispersion. Second, the Al$_4$Sr phase possesses a relatively high hardness, and therefore, hardness increases monotonically with increasing Sr content (see Figure 11).

The reinforcement particle–matrix interface critically influences the tensile strength of MMCs, and a high volume fraction, or a large particle can lead to interfacial debonding with an accompanying decrease in tensile strength. In related studies, Wang *et al.*[57] show that the yield strength and tensile strength of a SiC-reinforced Al-Cu composite decrease, while the hardness values of the composites increase with the increasing volume fractions of particles, and attribute this behavior to interfacial debonding. Thus, not only volume fraction, but also the size and morphology of reinforcing particles, exerts influence on mechanical behavior.[58] For example, the strength of particle-reinforced MMCs containing coarse-reinforcing particulates is lower than that of those containing fine particles.[58–60] A related study by Wang *et al.*[61] shows that the yield strength and UTS of a SiC reinforced Al-Cu composite reinforced with 4.7 μm particles are higher than those of composites reinforced with 77 μm particles. Moreover, the strength of AZ91D Mg alloy composites reportedly increases as reinforcement size is decreased.[62] On the basis of Enhanced Dislocation Density (EDD) models, the strengthening mainly depends on the reinforcing particles size and only mildly on the volume fraction.[63–65] The strength of the composites can be estimated using the following equation[66]:

$$\sigma = \sigma_m(1 + f_d)(1 + f_1) \qquad [4]$$

where σ is the enhanced strength of the composite; σ_m is the strength of the unreinforced matrix; f_d and f_1 are improvement factors associated, respectively, with the dislocation strengthening of the matrix and the load-bearing effect of the reinforcement. $f_d \propto \sqrt{\rho}$ and $\rho \propto \frac{1}{d}$ where d is a characteristic distance such as the particle diameter.[67] Therefore, particle size critically influences strength, and a smaller particle size generally leads to

higher strength. In addition, the load-bearing capacity of the reinforcement particles is related to their spatial distribution as load transfer from the matrix to the particles occurs more readily when the particles are homogeneously distributed in the matrix, a homogenous distribution of particles is likely to induce more significant strengthening. Hence, the particle size and spatial distribution of Al₄Sr will influence the mechanical behavior of LA93-xSr alloys. In the case of a constant Sr content, and accordingly unchanged Al₄Sr volume fraction, if the Al₄Sr particles are finer and the distribution of the particles is more homogeneous, then the strengthening effect is more pronounced. However, in the extruded LA93-xSr alloys, when the content of Sr exceeds 2.5 wt pct, the volume fraction and particle size of reinforcement particle Al₄Sr phase increase, and the distribution of Al₄Sr becomes inhomogeneous which leads to the decrease of tensile strength.

3. *A comparison of mechanical properties between as-cast and extruded LA93-xSr alloys*

The yield strength of extruded LA93 increases by 108.8 ± 3.2 pct, whereas that of LAJ932 alloys increases by 48.3 ± 4.0 pct as a result of extrusion. In a previous study,[51] we showed that the yield strength increases by 62.3 ± 2.6 pct in the as-cast LA93 alloys with 2.5 wt pct Sr. However, the yield strength of the extruded LAJ932 alloy containing 2.5 wt pct Sr only increases by 18.3 ± 4.7 pct compared to that of extruded LA93 alloy. The reasons for these difference are discussed as follows. For the as-cast alloys, the addition of Sr will lead to, not only grain refinement, but also the formation of Al₄Sr particles which effectively behave as strengthening particles. Thus, the influence of Sr on the mechanical behavior of the as-cast alloys can be considered by taking into account two factors. One is grain refinement, and the other is the formation of the strengthening Al₄Sr phase. However, the grains of LA93-xSr alloys are refined during extrusion, although the amount of Sr does not affect the grain size of α-Mg or β-Li phases in the extruded LA93-xSr alloys. Thus, the influence of Sr on the mechanical behavior of the extruded alloy can be rationalized solely on the strengthening characteristics of Al₄Sr, that is its size, volume fraction, and spatial distribution.

V. SUMMARY

1. LA93-xSr alloys contain both α-Mg (hcp) and β-Li (bcc) matrix phases. The α-Mg phase consists of primary α-Mg and eutectic α-Mg phase. In the as-cast LA93-xSr alloys, the primary α-Mg grains are from ~100 to 140 μm in size, while the eutectic α-Mg grains are ~3 μm in size. β-Li phase has both equiaxed grain with a diameter of ~1 μm and rod-like grains ~1 μm in diameter and ~5 to 10 μm in length.
2. Extruded LA93 alloy is composed of α-Mg, β-Li, and Mg₁₇Al₁₂ phases. The Al₄Sr phase is formed with the addition of Sr and is mainly distributed at the α/β phase interfaces and in eutectic regions. The grains in the extruded alloys are much finer than

those in the as-cast alloys. The effect of Sr on the grain size in the extruded alloys is not significant. CDRX occurs in α-Mg phase, while DDRX operates in β-Li phase during the hot extrusion process. α-Mg phase and Al₄Sr phase promote the DDRX of β-Li phase.
3. Dynamic recrystallization leads to refinement of the LA93-xSr grains during extrusion, and mechanical behavior is significantly improved by extrusion because of grain refinement and dislocation strengthening.
4. With increasing Sr, the strength of extruded LA93-xSr alloys first increases and then decreases, and the elongation decreases, whereas the hardness increases. LAJ932 alloy has a favorable combination of strength and ductility with tensile strength of 235 MPa, yield strength of 221 MPa, and the elongation of 19.4 pct.
5. The fracture surfaces of extruded LA93-xSr alloys contain evenly sized dimples, indicating ductile fracture.

APPENDIX

See Appendix Figure 14.

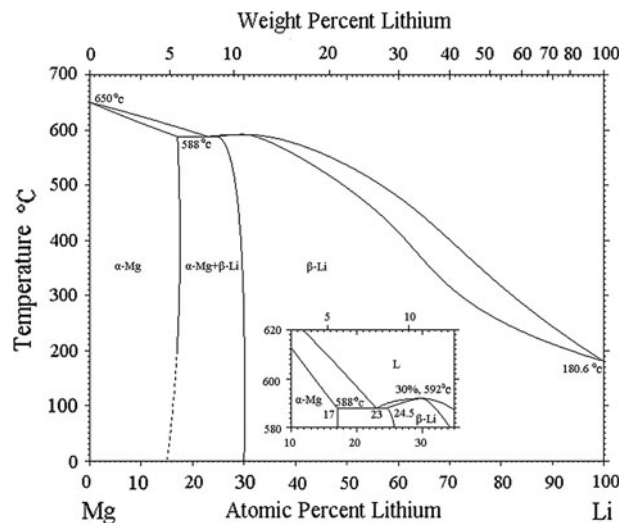

Fig. 14—Mg-Li binary phase diagram.

REFERENCES

1. H.W. Dong, L.D. Wang, Y.M. Wu, and L.M. Wang: *J. Alloys Compd.*, 2010, vol. 506, pp. 468–74.
2. M. Pekguleryuz, M. Celikin, M. Hoseini, A. Becerra, and L. MacKenzie: *J. Alloys Compd.*, 2012, vol. 510, pp. 15–25.
3. T. Wang, R.Z. Wu, M.L. Zhang, and J.Q. Li: *Mater. Sci. Eng. A*, 2011, vol. 528, pp. 5768–84.
4. J.M. Song, Y.H. Lin, C.W. Su, and J.Y. Wang: *Metall. Mater. Trans. A*, 2009, vol. 40A, pp. 1026–30.
5. H. Okamoto: *Desk Handbook: Phase Diagrams for Binary Alloys*, 1st ed., ASM International, Materials Park, OH, 2000.
6. M.J. Phasha, P.E. Ngoepe, H.R. Chauke, D.G. Pettifor, and D. Nguyen-Mannz: *Intermetallics*, 2010, vol. 18, pp. 2083–89.
7. H.Y. Wu, Z.W. Gao, J.Y. Lin, and C.H. Chiu: *J. Alloys Compd.*, 2009, vol. 474, pp. 158–63.
8. T.C. Chang, J.Y. Wang, C.L. Chu, and S.Y. Lee: *Mater. Lett.*, 2006, vol. 60, pp. 3272–76.
9. H. Takuda, S. Kikuchi, T. Tsukada, K. Kubota, and N. Hatta: *Mater. Sci. Eng. A*, 1999, vol. A271, pp. 251–56.
10. M.L. Zhang, R.Z. Wu, and T. Wang: *J. Mater. Sci.*, 2009, vol. 44, pp. 1237–40.
11. F.W. Bach, M. Schaper, and C. Jaschik: *Mater Sci. Forum*, 2003, vol. 419, pp. 1037–42.
12. B. Liu, M.L. Zhang, and R.Z. Wu: *Mater. Sci. Eng. A*, 2008, vol. 487, pp. 347–51.
13. X.R. Meng, R.Z. Wu, M.L. Zhang, L.B. Wu, and C.L. Cui: *J. Alloys Compd.*, 2009, vol. 486, pp. 722–25.
14. Z.K. Qu, R.Z. Wu, and M.L. Zhang: *Int. J. Cast Met. Res.*, 2010, vol. 23, pp. 364–67.
15. T. Wang, M.L. Zhang, and R.Z. Wu: *Mater. Lett.*, 2008, vol. 62, pp. 1846–48.
16. R.Z. Wu, Y.S. Deng, and M.L. Zhang: *J. Mater. Sci.*, 2009, vol. 44, pp. 4132–39.
17. B. Liu, M.L. Zhang, and Z.Y. Niu: *Mater. Sci. Forum*, 2007, vols. 546–549, pp. 211–16.
18. T. Liu, S.D. Wu, S.X. Li, and P.J. Li: *Mater. Sci. Eng. A*, 2007, vol. 460, pp. 499–503.
19. R. Chandran, T. Sakai, S. Kamado, Y. Kojima, and K. Matsuzawa: *J. Jpn. Inst. Light Met.*, 1998, vol. 48 (1), pp. 13–18.
20. A. Sadeghi and M. Pekguleryuz: *Mater. Charact.*, 2011, vol. 62, pp. 742–50.
21. M.B. Yang, F.S. Pan, X.F. Liang, J.S. Jia, and C.Y. Qin: *J. Mater. Sci.*, 2011, vol. 46, pp. 3216–24.
22. S.F. Liu and H. Wang: *Rare Met. Mater. Eng.*, 2006, vol. 35, pp. 970–73.
23. K. Hirai, H. Somekawa, Y. Takigawa, and K. Higashi: *Mater. Sci. Eng. A*, 2005, vol. 403, pp. 276–80.
24. T. Liu, W. Zhang, S.D. Wu, C.B. Jiang, S.X. Li, and Y.B. Xu: *Mater. Sci. Eng. A*, 2003, vol. 360, pp. 345–49.
25. F. Merlo: *J. Phys. F Met. Phys.*, 1988, vol. 18, pp. 1905–11.
26. A. Sadeghi, S. Shook, and M. Pekguleryuz: *Mater. Sci. Eng. A*, 2011, vol. 528, pp. 7529–36.
27. S. Gourdet and F. Montheillet: *Mater. Sci. Eng. A*, 2000, vol. 283, pp. 274–88.
28. M. Kawasaki, Z. Horita, and T.G. Langdon: *Mater. Sci. Eng. A*, 2009, vol. 524, pp. 143–50.
29. V.M. Segal: *Mater. Sci. Eng. A*, 1999, vol. 271, pp. 322–33.
30. H.M. Wen, Y.H. Zhao, T.D. Topping, D. Ashford, R.B. Figueiredo, C. Xu, T.G. Langdon, and E.J. Lavernia: *Adv. Eng. Mater.*, 2012, vol. 14, pp. 185–94.
31. T. Sakai, H. Miura, A. Goloborodko, and O. Sitdikov: *Acta Mater.*, 2009, vol. 57, pp. 153–62.
32. T.W. Fan, Q. Zhang, B.Y. Tang, L.M. Peng, and W.J. Ding: *Eur. Phys. J. B*, 2011, vol. 82, pp. 143–46.
33. H. Miuraa, M. It, X. Yang, and J.J. Jonas: *Mater. Sci. Eng. A*, 2012, vol. 538, pp. 63–68.
34. X. Yang, Y. Okabe, H. Miura, and T. Sakai: *Mater. Sci. Eng. A*, 2012, vol. 535, pp. 209–15.
35. S.B. Yi, S. Zaefferer, and H.-G. Brokmeier: *Mater. Sci. Eng. A*, 2006, vol. 424, pp. 275–81.
36. X. Yang, H. Miura, and T. Sakai: *Mater. Trans.*, 2003, vol. 44, pp. 197–203.
37. T.G. Langdon and R.Z. Valiev: *Prog. Mater Sci.*, 2006, vol. 51, pp. 881–981.
38. H.J. McQueen: *Mater. Sci. Eng. A*, 2004, vol. 387, pp. 203–08.
39. N. Dudova, A. Belyakov, T. Sakai, and R. Kaibyshev: *Acta Mater.*, 2010, vol. 58, pp. 3624–32.
40. H. Hallberg, M. Wallin, and M. Ristinmaa: *Comput. Mater. Sci.*, 2010, vol. 49, pp. 25–34.
41. Q. Ma, B. Li, E.B. Marin, and S.J. Horstemeyer: *Scripta Mater.*, 2011, vol. 65, pp. 823–26.
42. K. Hirai, H. Somekawa, Y. Takigawa, and K. Higashi: *Scripta Mater.*, 2007, vol. 56, pp. 237–40.
43. A. Belyakov, H. Miura, and T. Sakai: *ISIJ Int.*, 1998, vol. 38, pp. 595–601.
44. I. Salvatori, T. Inoue, and K. Nagai: *ISIJ Int.*, 2002, vol. 42, pp. 744–50.
45. G.Z. Quan, Y. Shi, Y.X. Wang, B.S. Kang, T.W. Ku, and W.J. Song: *Mater. Sci. Eng. A*, 2011, vol. 528, pp. 8051–59.
46. G.L. Ji, F.G. Li, Q.H. Li, H.Q. Li, and Z. Li: *Mater. Sci. Eng. A*, 2010, vol. 527, pp. 2350–55.
47. C.X. Yue, L.W. Zhang, S.I. Liao, J.B. Pei, H.J. Gao, Y.W. Jia, and X.J. Lian: *Mater. Sci. Eng. A*, 2009, vol. 499, pp. 177–81.
48. J.F. Devlin: *J. Phys. F Met. Phys.*, 1981, vol. 11, pp. 2497–2513.
49. J. Bai, Y.S. Sun, F. Xue, S. Xue, J. Qiang, and W.J. Tao: *Scripta Mater.*, 2006, vol. 55, pp. 1163–66.
50. Z. Chen, Z. Li, and C. Yu: *Mater. Sci. Eng. A*, 2011, vol. 528, pp. 961–66.
51. Y. Yang, X.D. Peng, W.D. Xie, Q.Y. Wei, G. Chen, and Z.H. Su: *Mater. Sci. Forum*, 2011, vol. 686, pp. 84–89.
52. W.J. Kim, I.K. Moon, and S.H. Han: *Mater. Sci. Eng. A*, 2012, vol. 538, pp. 374–85.
53. H.Y. Wang, X.L. Nan, N. Zhang, C. Wang, J.G. Wang, and Q.C. Jiang: *Mater. Chem. Phys.*, 2012, vol. 132, pp. 248–52.
54. M. Zimmermann, C. Stoumlcker, C. Muumlller-Bollenhagen, and H.J. Christ: *J. Phys. Conf. Ser.*, 2010, vol. 240 (1), pp. 1–4.
55. H.S. Kim: *Mater. Sci. Eng. A*, 2000, vol. 289, pp. 30–33.
56. M. Aljarrah, M.A. Parvez, J. Li, E. Essadiqi, and M. Medraj: *Sci. Technol. Adv. Mater.*, 2007, vol. 8, pp. 237–48.
57. Z.W. Wang, M. Song, C. Sun, D.H. Xiao, and Y.H. He: *Mater. Sci. Eng. A*, 2010, vol. 527, pp. 6537–42.
58. L.C. Davis, C. Andres, and J.E. Allison: *Mater. Sci. Eng. A*, 1998, vol. 249, pp. 40–45.
59. N. Chawla and Y.L. Shen: *Adv. Eng. Mater.*, 2001, vol. 3, pp. 357–70.
60. Y.S. Suh, S.P. Joshi, and K.T. Ramesh: *Acta Mater.*, 2009, vol. 57, pp. 5848–61.
61. Z.W. Wang, M. Song, C. Sun, and Y.H. He: *Mater. Sci. Eng. A*, 2011, vol. 528, pp. 1131–37.
62. R. Ajay and J.J. Lewandowski: *Mater. Sci. Eng. A*, 1996, vol. 220, pp. 85–92.
63. M. Vogelsang, R.J. Arsenault, and R.M. Fisher: *Metall. Trans. A*, 1986, vol. 17A, pp. 379–89.
64. R.J. Arsenault and N. Shi: *Mater. Sci. Eng.*, 1986, vol. 81, pp. 175–87.
65. R.J. Arsenault, L. Wang, and C.R. Feng: *Acta Metall. Mater.*, 1991, vol. 39, pp. 47–57.
66. N. Ramakrishnan: *Acta Mater.*, 1996, vol. 44, pp. 69–77.
67. C.W. Nan and D.R. Clarke: *Acta Mater.*, 1996, vol. 44, pp. 3801–11.